Matter

CellPress

Article

Structural heterogeneity governing deformability of metallic glass

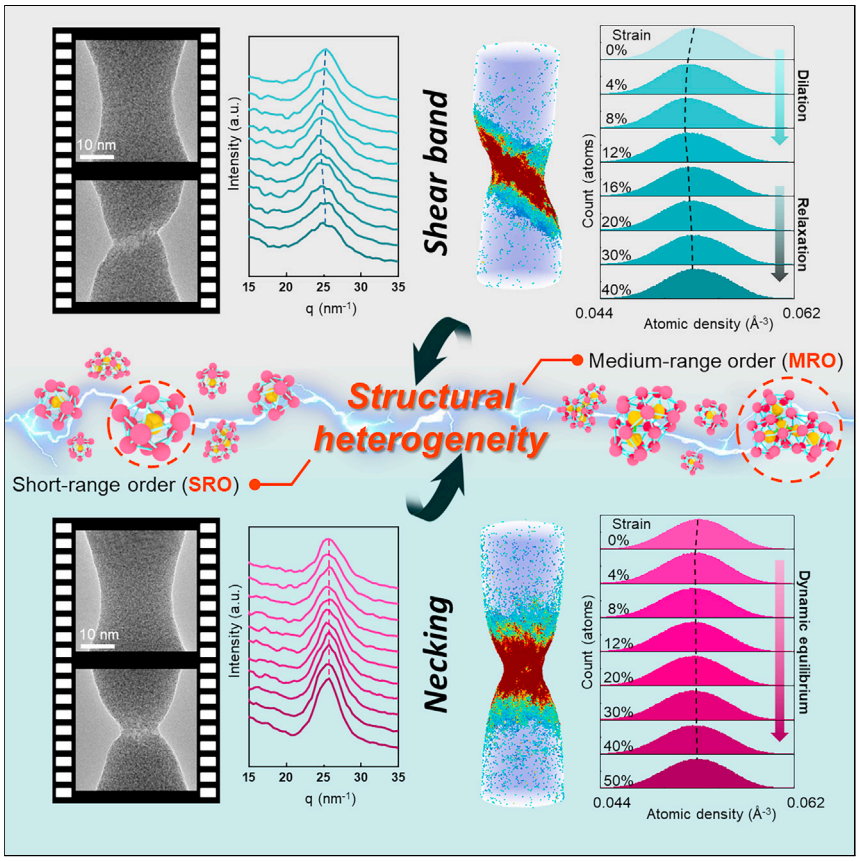

Hong et al. show that the deformability of metallic glasses is inherently determined by their structural heterogeneity, using monatomic Ta nanowires as an ideal platform. *In situ* transmission electron microscopy and atomistic simulations demonstrate visually that the microstructure motifs of metallic glasses can be tailored in a wide range, so different deformation modes can be activated. This work advances the understanding of structure-property relations of amorphous materials, which helps the design of amorphous nanomaterials with enhanced properties.

Youran Hong, Han Wang, Xing Li, ..., Penghui Cao, Robert O. Ritchie, Jiangwei Wang

zezhang@zju.edu.cn (Z.Z.)
caoph@uci.edu (P.C.)
roritchie@lbl.gov (R.O.R.)
jiangwei_wang@zju.edu.cn (J.W.)

Highlights

Microstructure of metallic glasses can be tailored in a wide range by electropulsing

Inherent structural heterogeneities determine deformation and fracture modes

Revealing the physical origin of processing history-dependent deformability

3 **Understanding**
Dependency and conditional studies on material behavior

Hong et al., Matter 6, 1160–1172
April 5, 2023
https://doi.org/10.1016/j.matt.2023.01.016

CellPress

Matter

Article

Structural heterogeneity governing deformability of metallic glass

Youran Hong,[1,6] Han Wang,[2,6] Xing Li,[1] Li Zhong,[3] Hangman Chen,[2] Ze Zhang,[1,*] Penghui Cao,[2,*] Robert O. Ritchie,[4,*] and Jiangwei Wang[1,5,7,*]

SUMMARY

Deformability of metallic glasses (MGs) is strongly influenced by their thermomechanical processing history that governs their energy state and local atomic configurations. Here, we reveal that monatomic tantalum MG nanowires, tailored by electropulsing, can attain a remarkable range of deformability, manifesting as either liquid-like flow or brittle fracture. Inherent structural heterogeneity on the level of atomic order dominates the plasticity and deformation transition of monatomic MGs. By tracking atomic rearrangement during straining, we find the dispersive and sparse distribution of local order is associated with necking, yet percolation of medium-range order constrains the deformability and results in brittle failure. This work sheds new light on the structure-property relationships in MGs, which has important implications for the design of nanoscale MGs with tunable mechanical properties.

INTRODUCTION

Metallic glasses (MGs) possess unique mechanical properties, including ultra-high strength and excellent elasticity.[1] On yielding, however, MGs generally suffer from poor ductility due to highly localized inhomogeneous deformation from the formation and propagation of a few dominant shear bands.[1,2] Significant efforts have been made to enhance the deformability and thus ductility of MGs by varying thermomechanical processing.[3] Analogous to crystalline metals and alloys, changes in fabrication and/or processing history, e.g., in terms of cooling rate, aging, or "energy injection," can endow MGs with a wide range of inherent metastable states,[3] corresponding to numerous metabasins in their potential energy landscapes. For a given MG, specific variations in their processing history,[4,5] a reduction in sample size,[6–8] and even irradiation[9] can facilitate, to some extent, homogeneous plastic flow to induce a brittle-to-ductile transition. Such a transition in deformation mode has often been ascribed to the so-called "rejuvenation" of MGs,[3] although its microstructural origin remains largely elusive.

In classical theory,[3] such history-dependent behavior of MGs has mainly been ascribed to the formation of different metastable states with distinct atomic packing and thus mechanical responses. Rejuvenation was believed to reduce the atomic packing density and increase the free volume of MGs,[10–13] thereby facilitating the formation of shear transformation zones (STZs) and enhancing the ductility.[14] However, previous studies merely presented the statistically averaged volume information in bulk MGs via diffraction peak analyses,[10–13] especially the first sharp diffraction peak (FSDP, an essential structural characteristic and indicator of amorphous density denoted as q_1), which cannot represent the intrinsic difference

PROGRESS AND POTENTIAL

Revealing the inherent structure-property relations in a broad class of amorphous materials is crucial for the design of metallic glasses (MGs) with controllable properties. Here, we show that the deformability of MGs is inherently determined by their structural heterogeneity, using monatomic Ta nanowires as an ideal platform. The monatomic MG nanowires largely eliminate the possible interference from chemistry heterogeneity. By applying nanosecond electropulsing inside transmission electron microscopy, the microstructure motifs and structural heterogeneity of MGs are tailored in a wide range, so ductile and brittle fracture modes are activated. Atomistic simulations demonstrate significant correlations between the brittle-ductile transition and the medium-range order in MGs. These results provide a unique perspective on manufacturing amorphous nanomaterials with enhanced properties for engineering applications.

between atomic configurations or their evolutions. At the atomic scale, MGs are composed of numerous structural heterogeneities, including short-range order (SRO) and medium-range order (MRO).[15,16] Their spatial distributions and dynamic evolution should directly correlate with the deformability of MGs, which have yet to be elucidated. Both *in situ*[17] and *ex situ*[18,19] characterizations demonstrated that the occurrence of local shear transformation and shear band formation in MGs is often accompanied by a significant reduction in MROs. During this process, considerable diversity in SROs/MROs is hypothesized to manifest as favored and unfavored local atomic configurations,[20,21] which, especially MROs, directly impact the mechanical response of MGs.[22] However, the impact of structural heterogeneities, particularly the differences in SROs and MROs and their dynamic evolutions, on the deformability and brittle-to-ductile transition of MGs remains an open question.

Here, we uncover the microstructural origin of the brittle-to-ductile transition of monoatomic tantalum (Ta) MGs nanowires using *in situ* nanomechanical testing and atomistic simulation. Monatomic MGs can largely eliminate the interference from chemical heterogeneity on the configuration of atomic clusters[10] and thus their effects on deformation dynamics. By applying nanosecond electric pulses,[23] we are able to tailor the microstructure motifs of MGs to induce different deformation modes (shear band or necking). By tracking the dynamic development of microstructure through selected-area electron diffraction (SAED) and high-resolution transmission electron microscopy (HRTEM), as well as large-scale molecular dynamics, we reveal the significant roles of structural heterogeneity in controlling the brittle-to-ductile transition in monatomic Ta MGs.

RESULTS AND DISCUSSION

Dynamic microstructural identification of plastic deformation of MG nanowires

We first decouple the elastic and plastic behaviors of Ta MG nanowires, by quantifying the FSDP via *in situ* SAED under tension. Ta MG nanowires with cylindrical (Figure 1A) and hyperboloidal (Figure 1B) shapes were fabricated and loaded (Figure S1 illustrates the initial morphologies). On loading, the cylindrical nanowire exhibited fast fracture at the upper end (Figure 1A), presumably due to a high stress concentration at the nanowire-substrate interface. In contrast, the interior of the nanowire remained primarily elastic. As shown in Figure 1C, the position in momentum transfer of the FSDP (q_1) can be seen to gradually shift to a lower value with the tensile strain, corresponding to a structural dilatation; immediately after fracture, the peak promptly shifts back to its nominally original position (inset in Figure 1C), indicating a full elastic recovery. The change in FSDP, consistent with the deformation mode, provides benchmarks of essential transitions in our *in situ* straining experiments. In the hyperboloidal sample (Figure 1D), the FSDP shifted slightly toward a lower q similarly during the early stage of deformation; subsequently, the peak gradually shifted back toward a higher q, in particular during the late stage of deformation, which suggests the occurrence of a densification process (relaxation) that predominates over the dilatation. With the strain localization in the necking zone, a shear-dominated fracture occurred at the minimum cross-section of the sample (Figure 1B), leaving a rough fracture surface. After fracture, the FSDP further rebounded toward a higher q, indicative of elastic recovery and the resultant densification in the elastically-deformed regions. Interestingly, a secondary peak with large q_1 appeared after fracture (inset in Figure 1D), implying significant peak broadening due to complicated microstructure changes induced by localized deformation and inhomogeneous distributed residual stress in the fracture region.[24] In both samples, no crystallization appears throughout the entire deformation process (Figure S2). A

[1]Center of Electron Microscopy and State Key Laboratory of Silicon Materials, School of Materials Science and Engineering, Zhejiang University, Hangzhou 310027, P. R. China

[2]Department of Mechanical and Aerospace Engineering, University of California Irvine, Irvine, CA 92697, USA

[3]SEU-FEI Nano-Pico Center, Key Laboratory of MEMS of Ministry of Education, Southeast University, Nanjing 210096, P. R. China

[4]Department of Materials Science and Engineering, University of California Berkeley, Berkeley, CA 94720, USA

[5]Institute of Materials, Henan Academy of Sciences, Zhengzhou 450046, China

[6]These authors contributed equally

[7]Lead contact

*Correspondence: zezhang@zju.edu.cn (Z.Z.), caoph@uci.edu (P.C.), roritchie@lbl.gov (R.O.R.), jiangwei_wang@zju.edu.cn (J.W.)

https://doi.org/10.1016/j.matt.2023.01.016

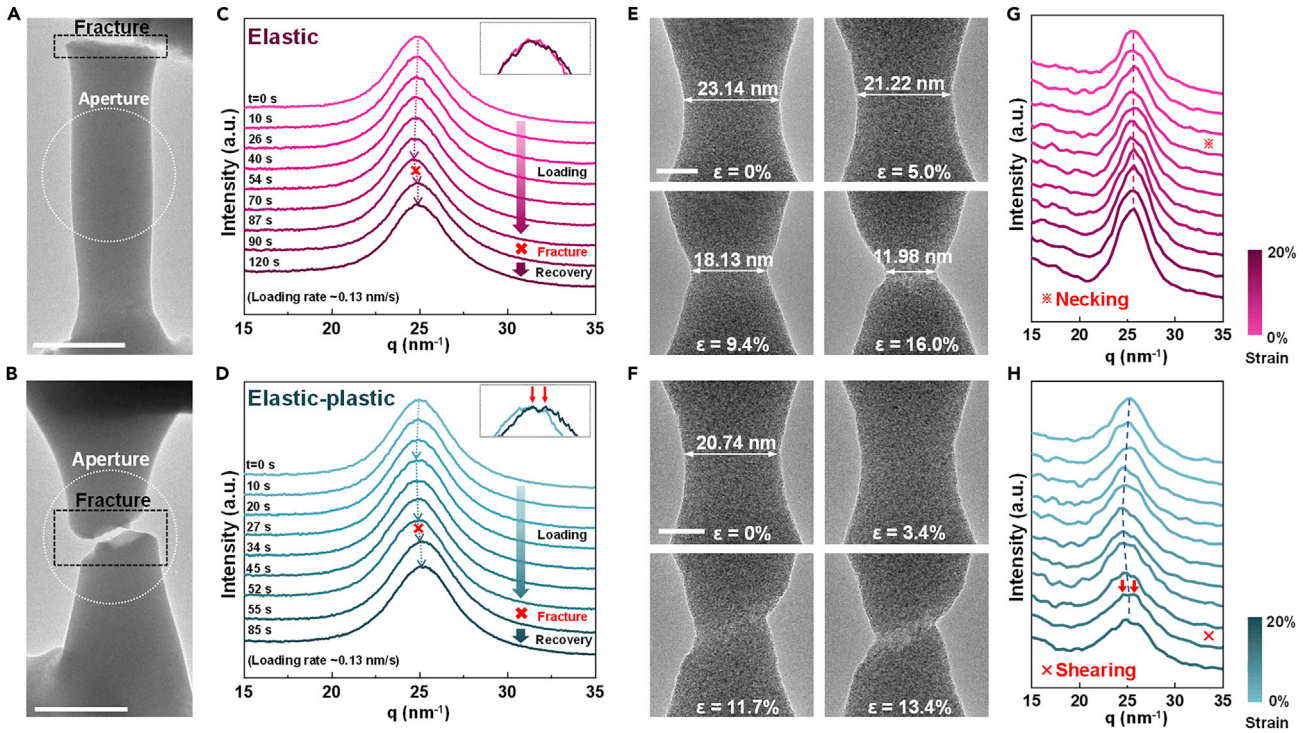

Figure 1. Deformation behaviors of Ta MG nanowires

(A and B) TEM images showing the fracture morphology of two different samples. Diffraction information is acquired within the selected-area aperture denoted by the white dashed circles.

(C and D) SAED profiles over time of these two nanowires obtained *in situ* during the deformation, focusing on the evolution of the first sharp diffraction peak (FSDP). There are three stages for the cylindrical sample: elastic deformation (0–87 s), fracture (87–90 s), and elastic recovery (90–120 s); four stages for the hyperboloidal sample: elastic deformation (0–27 s), plastic deformation (27–52 s), fracture (52–55 s), and recovery (55–85 s). Insets compare the magnified features of the first diffraction peak between the initial (light color) and fractured (dark color) states.

(E and F) Deformation snapshots of two tension-loaded Ta MG nanowires with a similar size but different processing histories.

(G and H) Evolution of the azimuthally averaged one-dimensional fast Fourier transform (FFT) intensity of these two nanowires during deformation, respectively. The dashed curves are provided as a reference for tracking the change in the peak positions. Scale bars: (A and B) 100 nm; (E and F) 10 nm.

comparison between the change in the FSDP during elastic and plastic deformation clearly suggests the presence of two competing processes actively involved in the deformation of the MGs: stress-driven structural dilatation and local atomic rearrangement-mediated densification. Both processes are closely related to the configurational evolution of atomic clusters, whereas the initial energy state of the MGs appears to determine the predominance of the two processes and thus the overall deformation behavior.

To further reveal the microstructural origin underlying the different deformation modes, we attempted to tune the atomic structures of the monatomic Ta MG nanowires to various energy states through the use of electropulsing. Specifically, we reduced the size of the test samples to enhance the current density passing through them, in order to improve the extent of pulse-induced structural variations. With the size reduction, an as-welded MG nanowire (~23 nm in diameter, obtained by single-pulse nano-welding) exhibited interesting viscous flow from plastic (necking) instability under tension (Figure 1E and Video S1). This behavior is in stark contrast to the shear localization seen in the larger-sized nanowires. Clear neck development and viscous flow are an indication of an intense process of atomic rearrangement.[25] An annealed Ta MG nanowire with fully amorphous structure (Figure 1F) was

obtained by multiple small pulse processing after fabrication (see Experimental procedures for details). Although this nanowire had a similar, or even slightly smaller, diameter (~21 nm) than the samples described above, it displayed limited ductility in terms of failure via a single significant shear band (Figure 1F) in contrast to the severe necking in Figure 1E. The shear band formation is shown in Video S2, where a small degree of plastic flow can be detected.

To evaluate the dynamic structural evolution during straining, we analyzed the fast Fourier transform (FFT) patterns of sequential deformation images. For the nanowire fractured by necking (Figure 1E), the position of the maximum peak (q_1) fluctuated throughout the tensile test, without any apparent directional shift (Figure 1G). This feature of a dynamic equilibrium of the average atomic volume suggests that the two processes of dilatation and densification are in balance in the deforming nanowire. By contrast, the pulse-annealed nanowire that displayed a shear band fracture exhibited an obvious peak shift during deformation toward the low q side (Figure 1H, dilation predominated process). However, when the shear band formed, the peak shifted back quickly, followed by a peak split (marked by the red arrows in Figure 1H). These phenomena shown in Figure 1H in general are consistent with the SAED experiment presented in Figure 1D; together they present a clear characterization of the microstructural dynamics during inhomogeneous plastic shear of MGs. Specifically, a statistical dilation of the average atomic volume occurs first under tension, associated with a continuous rearrangement of atomic clusters at the atomistic scale; the subsequent formation of a shear band then effectively releases elastic strain energy, to induce the relaxation of energetically unfavored atomic clusters. Until failure occurred, shear band formation was accompanied by a more evident peak broadening from inhomogeneous strain than necking (Figure 1H). These two nanowires had a similar size and were deformed under identical conditions; accordingly, the contribution to the deformation from size- and surface-induced atomic flow should be similar. Additionally, the two nanowires had almost identical q_1 (~25.4 nm^{-1}) values, i.e., the same average atomic volume. These facts strongly imply that the marked difference observed in their plastic deformation behavior must have originated from another important structural characteristic, specifically, the intrinsic structural heterogeneity in MGs.

Atomistic modeling of Ta MG nanowires from brittle to ductile

Accordingly, large-scale atomistic simulations were performed to explore the critical role of structural heterogeneity on the deformation of the Ta MG nanowires. Two samples with the same size but markedly different processing histories, including aging that creates a highly relaxed state corresponding to the pulse-annealed nanowire and rejuvenation that generates an ultra-fast quenched state corresponding to the as-welded nanowire, were prepared for mechanical testing. In the aged nanowire (Figure 2A), the simulations show that local shear transformation events (STZs) were activated upon deformation, which accumulated gradually to form an incipient shear band at 16% strain. At the strain of 30%, a mature shear band was developed through increasing activation and percolation of the shear transformation events. In contrast, the triggered STZs in the rejuvenated nanowire spread uniformly at strain level below 30%, which gave rise to an enhanced ductility accompanied by the delayed necking localization at 50% strain (Figure 2B). The spatial and temporal evolutions of local plastic strain demonstrate a clear brittle-to-ductile transition from the aged nanowire (shear banding) to the rejuvenated one (necking-like flow). Figures 2C and 2D provide further quantification of the dynamic variations in the distribution of the atomic density, i.e., the inverse of atomic volume enclosed by the Voronoi cell of the central atom (further discussion of this is provided in Note

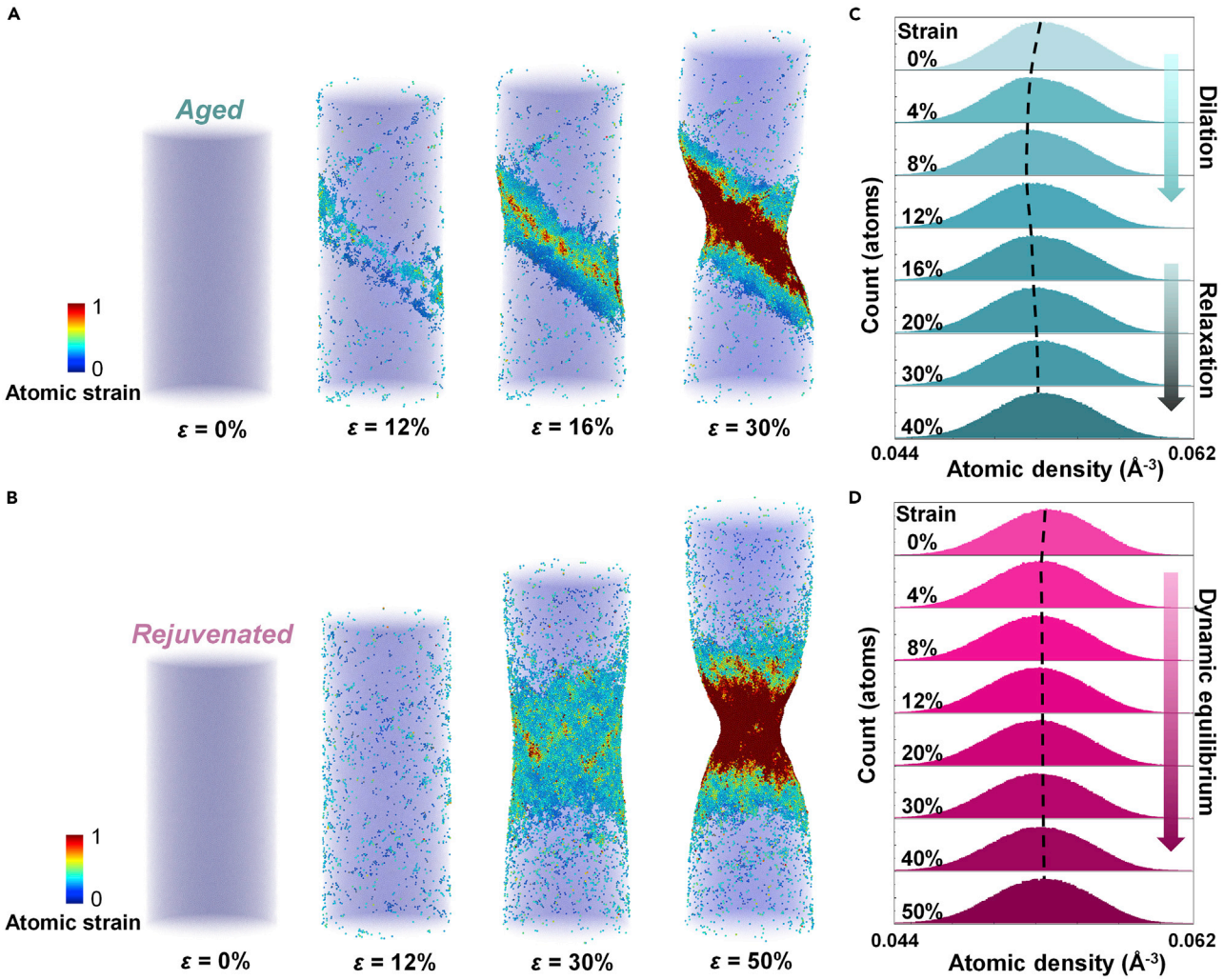

Figure 2. Simulations of the deformation behaviors of aged and rejuvenated Ta MG nanowires

(A and B) The structural evolution of the aged (A) and rejuvenated nanowires (B) with straining, respectively. The atoms are (false) color-coded by the atomic strain; only the atoms with atomic shear strain higher than 0.3 are shown.

(C and D) The evolution of the distribution of the local atomic density with strain in aged (C) and rejuvenated nanowires (D). The dashed black lines indicate the peak position of the distribution.

S1). In the aged nanowire, the peak position of the atomic density gradually shifted to a smaller value prior to a 12% strain (Figure 2C), implying the occurrence of a stress-induced dilation and free volume accumulation during elastic deformation. Immediately after the yielding, at the formation of an incipient shear band at 16% strain, the decreasing trend in the peak in atomic density appeared to reverse with further increase in strain up to 40%, indicating that the applied strain had been accommodated in the shear band to enable the relaxation of the elastically deformed matrix. In contrast, for the rejuvenated nanowire, the peak in atomic density displayed no such variation with strain (Figure 2D), suggesting the existence of a relaxation process that can densify the structure and compensate for any dilation. A similar variation of peak profile with strain in aged and rejuvenated systems is also observed in our molecular dynamics (MD) deformation simulations (Figure S3). These simulation results are remarkably consistent with the experimentally measured distributions in the peak in atomic density in Figure 1; this implies a strong

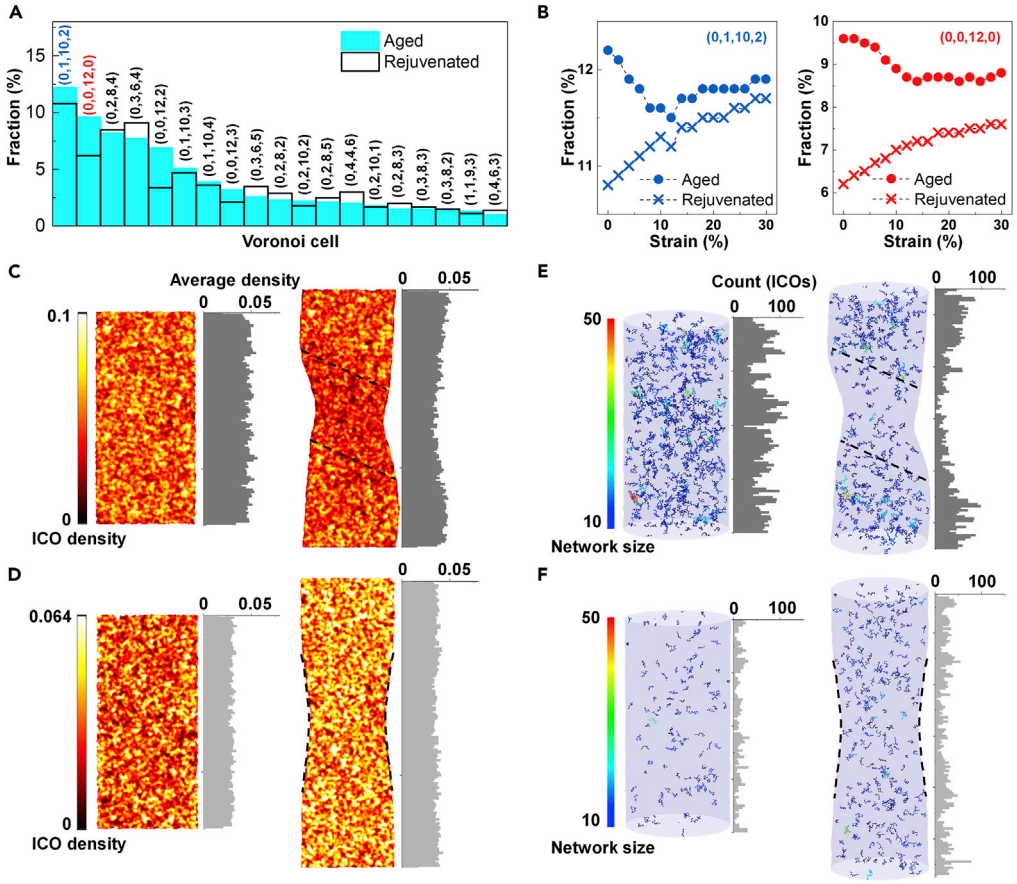

Figure 3. Short-range and medium-range order in aged and rejuvenated Ta MG nanowires

(A) Distributions of Voronoi polyhedra with a fraction greater than 1% in aged and rejuvenated nanowires, respectively.

(B) Evolution of the fraction of (0,1,10,2) distorted icosahedra (blue) and (0,0,12,0) perfect icosahedra (red) as a function of applied strain in aged (solid circles) and rejuvenated (crosses) nanowires.

(C) 2D spatial distribution of the density of icosahedra (ICO) in aged nanowires at 0% strain (initial structure) and 25% strain (shear band formation).

(D) 2D spatial distribution of the ICO density in rejuvenated nanowires at 0% strain (initial structure) and 35% strain (necking formation).

(E and F) The corresponding distributions of medium-range order in these two nanowires, as illustrated by the 3D spatial distribution of ICO networks connected by volume sharing. Only ICO networks with more than 10 atoms are shown; they are shown (false) colored by network size.

correlation between local atomic structure and the overall deformation behavior of MGs. Additionally, both nanowires possess a similar average atomic volume of 18.90 $\pm$ 0.01 Å^3, close to the same average q_1 value in Figure 1. Given the completely different deformation modes in these two types of nanowires, it is reasonable to speculate that the atomic free volume per se, or the q_1 value, should not be considered as the determining microstructural feature controlling the mechanical response of MGs.

To elucidate the physical origin of brittle-to-ductile transition in the Ta MG nanowires with the same average atomic volume, the evolution of atomic structure based on SRO and MRO was carefully analyzed. The SRO is characterized in terms of Voronoi polyhedra (Figure S4), which represents the elemental building units that comprise the amorphous structure.[15] The connectivity of the polyhedra, via vertex, edge, face, or volume sharing, reflects the medium-range arrangements in MGs[16,26] (as discussed in Note S2 and Figure S5). Figure 3A presents and compares the statistical distributions of Voronoi polyhedra in the undeformed MG nanowires. The aged nanowire has a more concentrated distribution with high fractions of certain

groups of polyhedra (irrelevant to the volume of Voronoi cells, per Figure S6); in contrast, the rejuvenated nanowire exhibits a relatively random distribution, suggesting the thermal-induced propensity for structural homogeneity. In particular, the dense icosahedron (ICO) (0,0,12,0) and icosahedral-like (0,1,10,2) atomic motifs, which are the two most energetically favored local atomic configurations in the aged nanowire, are appreciably reduced after rejuvenation; indeed, they are not the most preferred form of SRO in rejuvenated nanowire. Given that the mean atomic volumes associated with polyhedral and their distribution are the same in these two samples (Figure S7), the fluctuation in the proportion of specific polyhedra, as well as the dynamic transformation between different types of Voronoi cells during straining (Figure S8), should provide the root cause for the variation in atomic volume distribution in the respective systems plotted in Figures 2C and 2D. Figure 3B shows the fractions of energetically favorable icosahedral-like motifs, i.e., (0,1,10,2) and ICO (0,0,12,0), as a function of the applied strain. Strikingly, the aged and rejuvenated systems demonstrate distinct behaviors in the early stage of deformation: the former involves a decrease in the fraction of icosahedral-like packing, yet the latter exhibits an increase in this fraction. The strain-induced accumulation of energetically preferred clusters in the rejuvenated nanowire indicates structural relaxation and the resultant formation of lower energy clusters during mechanical loading.

Figures 3C–3F present the spatial evolutions of ICO clusters (SRO) and their networks (MRO) in response to the mechanical strain, with the objective to connect them with the necking and shear band activities. In the aged system (Figure 3C), the density of ICOs is appreciably reduced in the shear band region, indicating that the local plastic deformation associated with shear banding formation would destroy the ICO packing (Figure S9A and Video S3). Regarding the rejuvenated nanowire (Figure 3D), however, the ICOs tend to nucleate throughout the whole system, suggesting a strain-mediated homogeneous relaxation (Figure S9B). In Figures 3E and 3F, we show the spatial evolution of ICO networks (MRO) that are comprised of volume-shared ICOs. It is noted that the ICO networks are drastically reduced along with the shear bands (right panel of Figures 3E and S10A and Video S4). We further analyzed the statistical distribution of isolated ICO and connected ICOs (Figure S11) in the aged and rejuvenated systems. Interestingly both nanowires show nearly the same amount of isolated ICOs, but the aged system possesses more ICO-connected clusters (network). During mechanical straining, the ICO networks can be seen to be shrinking in the aged system, yet they are growing in the rejuvenated system, although the number of isolated ICOs remains essentially unchanged. This signifies that the ICO networks (i.e., MROs) are primarily responsible for plastic deformation and for the observed brittle-to-ductile transition; as such, we can conclude that they dictate the deformability and mechanical response of the MG nanowires. It is also important to note that thermal annealing could easily reduce the energy of MGs at the rejuvenated state by the rearrangements of atoms.[27,28] To differentiate the strain effect from the thermal effect, we tracked how the distribution of ICOs and MROs was evolving in the rejuvenated sample during thermal annealing. As shown in Figure S12, the thermal relaxation has a negligible impact on the accumulation of MRO, compared with the ones in the uniaxially loaded sample.

Considerable structural heterogeneity in monatomic MG nanowires

For amorphous materials, the topological structural order determines the configurational potential energy[29] where, with the accumulation of order, a hierarchical structural heterogeneity is generated. As a representative feature with 5-fold symmetry and low potential energy, ICO ordering is prone to aggregate and connect to

form long ICO chains and dense networks under slower cooling or thermal aging,[20] reflecting a typical process of how SROs organize themselves into MROs. These interlocked chains and networks build the backbone of stiff MGs, and their spatial distributions should dominate the mechanical response of MGs. Meanwhile, frustrated atomic clusters with higher configurational potential energy fill up the space framed by the backbones and "glue" them together. The stiff ICO network and its surrounding soft matrix respond differently to external loading, so the structural heterogeneity spawns deformation heterogeneity. When the ICOs are percolated to form highly connected stable MROs, as in a well-aged system, they restrict or resist the structure relaxation of atomic clusters within or around them, local shear transformation events break the ICOs, and the corresponding transformation of the polyhedra results in volume expansion; thus, MROs such as ICO networks provide an ideal location for free volume accumulation or STZ activation and propagation. In contrast, if the ICOs are spatially isolated, the MROs become fewer and looser, so their constraint on the mobility of atoms is weakened. Consequently, when shear transformation and local rearrangement occur in extensive soft regions, the formation of new ICOs or MROs results in relaxation and densification. This MRO-controlled plastic deformation of MGs is consistent with our *in situ* HRTEM observations (Figure S13), where crystal-like MROs are generated in the necking sample but are broken down in the shear band sample. To summarize, the structural heterogeneity, stemming from various relative fractions and spatial distribution of SRO and MRO, which in turn depends on the processing history, determines the deformation behavior of MG nanowires.

To further verify the dominance of structural heterogeneity on the deformation of MGs, we further processed Ta MG nanowires to an extreme state of structural heterogeneity, consisting of nanograins embedded in a glass matrix. Figures 4A and 4B illustrate an example of this glass nanowire with crystal seeds. Both the FFT pattern (inset in Figure 4A) and HRTEM observations (Figure 4B) clearly indicate the extensive existence of numerous crystallographic lattices in the amorphous matrix. Compared with its initial fully amorphous state (Figures S14A–S14D), the partially crystalized nanowire exhibits a sharper peak on its azimuthal average FFT profile (Figure 4C), associated with extensive but dispersed ordered regions (Figure 4B). Under tension, apparent brittle fracture occurred at a strain of 5.5% (shown in Video S5 and the inset in Figure 4D), which implies insignificant strain-induced relaxation processes, according to its FFT profile distribution (Figure 4D). Compared with the nanowires in Figures 1 and S15, the shear fracture of the partially crystalized nanowire further illustrates that structural heterogeneity should be the intrinsic factor determining the plastic deformation mode of MGs, in contrast to the widely believed variation of averaged structural state.[30] Figure 4E summarizes the deformation behavior of Ta MG nanowires with different average q_1 values and sizes. The q_1-independent fracture modes validate that the deformation mode of MGs is not determined by the average q_1 (free volume) but its inherent structural heterogeneity. Note that as the q_1 value represents an average structure parameter associated with average atomic volume or free volume, it cannot reflect exactly the intrinsic structural heterogeneity of MGs, which determines their deformation modes. In other words, samples with the same q_1 values may possess different arrangements and combinations of SROs/MROs. Furthermore, the degree of structural ordering is not closely related to the q_1 value, but rather the full widths at half maximum (or the sharpness of peak). As an aside, it is important to note that the size-dependent brittle-to-ductile transition in MGs has been widely studied,[31,32] where smaller MG samples have fewer flaws for the shear band initiation and thereby enhance the ductility via uniform STZ or diffusion-controlled mechanisms.[33–35] Our contention here, however,

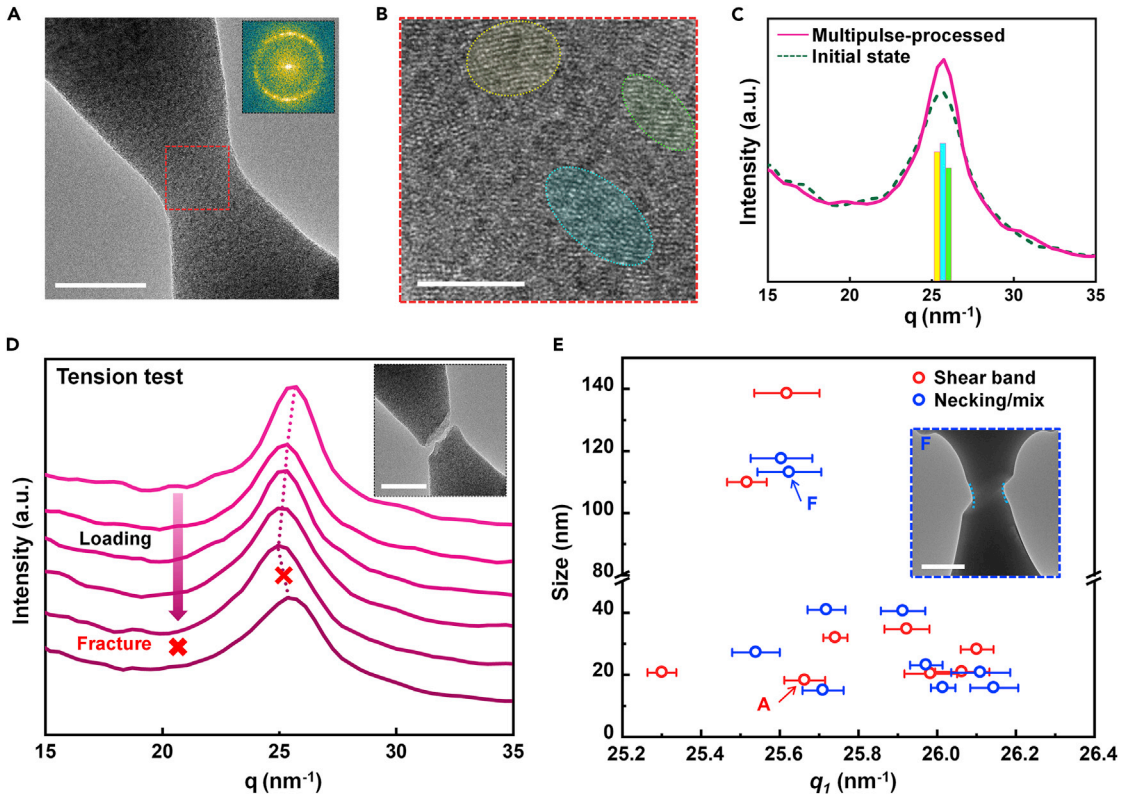

Figure 4. Effect of structural heterogeneity on the deformation of Ta MG nanowires

(A) A Ta MG nanowire with crystal seeds. The FFT pattern confirms the existence of crystal seeds.

(B) HRTEM image showing visible nanocrystals in the amorphous matrix in the selected area of (A).

(C) Azimuthally averaged one-dimensional FFT profiles from the selected area of (A) at initial state and after multipulse process, respectively. Three columns represent the corresponding color regions in (B), where their positions and heights correspond to lattice spacings and region areas, respectively.

(D) Evolution of FFT profiles from the strain concentration area during the tension test. Inset is the fracture morphology of the nanowire.

(E) Distribution of fracture modes of Ta MG nanowires with different q_1 values and sizes. The error bars are the standard errors of fitting parameters. Inset (F) shows a mixed fracture of a larger specimen. Scale bars: (A) 20 nm; (B) 5 nm; (D) 20 nm; (F) 100 nm.

is that the size effect inevitably works on the structural heterogeneity and promotes the cluster rearrangement in our small samples; thus, the free volume is easier to redistribute or escape (for an example, see Figure S15). Accordingly, our results on the shear fracture of Ta MG nanowires sized less than 20 nm (Figure 4E) demonstrate that the size effect merely acts as a secondary factor on the brittle-to-ductile transition of MGs, with the intrinsic structural heterogeneity of MGs playing the dominant role in determining the deformation modes. This implies that it is feasible to use electropulsing to tailor structural heterogeneity in amorphous materials to improve the room temperature tensile ductility in larger MG samples (Figure 4F). Note that though nanosecond electropulsing process provides a possibility of manipulating the microstructural heterogeneity in MGs, the precise operation can be influenced by several factors, including sample geometry, pulse parameter, and number of pulses applied.

Conclusions

In conclusion, we reveal in this study the origin of the brittle-to-ductile transition in monatomic Ta MGs, by tailoring the intrinsic structural heterogeneity via electropulsing and tracking their dynamic evolution upon deformation. The structural heterogeneity is found to be an intrinsic factor in controlling the deformation modes of

monoatomic MG nanowires, which provides direct experimental evidence of the origins of the deformability of MGs, in contrast to the widely accepted averaged structural state criterion.[3,30] Atomistic simulations further demonstrate that the origin of the brittle-to-ductile transition in Ta MG nanowires is more associated with the structural features of MRO rather than with SRO. These findings establish critical correlations between the inherent structure of metallic glasses and their deformation modes, which we believe advances the current understanding of structure-property relations in a broad class of MG materials. Further, this study is of technological importance for the future design of MGs with controllable mechanical properties.

EXPERIMENTAL PROCEDURES

Resource availability

Lead contact

Further information and requests for resources and reagents should be directed to and will be fulfilled by the lead contact, Jiangwei Wang (jiangwei_wang@zju.edu.cn).

Materials availability

This study did not generate new unique reagents.

Data and code availability

All data are available in the main text or the supplemental information.

Specimen preparation and *in situ* tensile straining

Two bulk Ta rods (99.9+ wt %), supplied by Alfa Aesar, with a 0.25 mm diameter, were cut with diagonal-cutting pliers to form fresh fracture edges with plentiful triangular nano-tips. To minimize possible contamination prior to cutting, the rods were stored in a glove box filled with helium (with O_2 and H_2O levels both below 1 ppm) after ultrasonic cleaning in absolute ethyl alcohol and drying overnight *in vacuo* at 120°C before cutting. Subsequently, two fractured Ta rods were mounted onto the fixed end and to the probe side of a PicoFemto TEM-STM specimen holder (Zeptools Co.). *In situ* nanofabrication and tensile straining of these Ta MGs were then performed inside a Cs-corrected FEI Titan G2 60–300 transmission electron microscope (TEM) operating at 300 kV. During nanofabrication, the Ta rod on the probe side was moved via a built-in piezo-manipulator to approach the rod at the fixed end of the holder in order to bring the two selected nano-tips into contact. After applying a transient square electric pulse (1.0–3.0 V, 5 ns) by a Pulse Generator (Agilent Technologies model 81110A), the Ta MG nanowires were subjected to ultra-fast quenching after nano-welding of the tips. Tensile straining of the as-fabricated Ta MG nanowires was performed by retracting the Ta rod at the probe side at a strain rate of $\sim 10^{-3}$ s^{-1}. During deformation, SAED patterns were monitored *in situ*, using a diffraction lens aperture holder of ~200 nm. The TEM images, SAED patterns, and associated videos were all recorded by a GATAN Model 994 charge-coupled device camera at an exposure time of 0.3–0.5 s (per frame). In Figure 4E, nanowires with different q_1 were fabricated by applying different electropulsing treatments, specifically by changing the pulse parameters and number of pulses applied.

As electron beam irradiation can influence the deformation of MGs, a low irradiation dose of 100–200 $eÅ^{-2}$ s^{-1} as well as beam blank experiment were applied to minimize this possibility. For direct comparisons, the same beam condition was employed for nanowires of similar size, in order to reduce the possible contributions from knock-on damage and surface diffusion to their deformation (see Figures 1E–1H). It should be noted though that as Ta has a relatively large atomic weight, any

knock-on damage would likely be weak owing to its ultra-high knock-on thresholds. Additionally, electron beam heating was deemed to be negligible because of the high thermal conductivity of Ta and the fact that the e-beam dose was limited.

Structure analysis based on SAED and FFT

For SAED analysis, the magnitude of the scattering vector was defined as $q = (4\pi/\lambda)\sin\theta$, where θ is the scattering half-angle, and λ is the electron wavelength. For HRTEM analysis, the FFT results can provide statistical information on the atomic arrangements, akin to diffraction patterns. The azimuthally averaged scattered intensity (from SAED) and FFT intensity (from HRTEM) were computed using the eRDF Analyser software.[36] Specifically, two-dimensional (2D) FFT patterns were acquired from sequential HRTEM images. Keeping the selected regions of FFT on the minimum section of the samples (256 × 256 pixels), the real-time azimuthal average variations of the FFT intensity were recorded. The azimuthally averaged HRTEM-FFT profiles were then smoothed using the Savitzky-Golay method in the OriginPro 2018 software.

Atomistic models and uniaxial tensile deformation of metallic glass nanowires

We used the embedded atom method[37] potential, previously developed to model amorphous Ta, for describing the interatomic interactions.[23] The initial bulk glass was simulated by quenching an equilibrated high-temperature liquid from 4,000 K down to 1 K at a finite cooling rate of 0.25 K/ps. The as-quenched glassy block was then tailored into cylindrical nanowires, 20 nm in diameter and 40 nm in length, containing approximately 6.56×10^5 Ta atoms. Starting from this prepared nanopillar, two independent simulations, for aging and rejuvenation, were instigated to prepare aged and rejuvenated nanowires, respectively. Specifically, the nanowire was relaxed at a temperature of 1,600 K (well below glass transition temperature of ~1,700 K), followed by slow cooling to 300 K, to generate the aged nanowire. The rejuvenated nanowire was acquired by heating the nanowire to 2,500 K for 50 ps, followed by fast quenching to 300 K. In order to eliminate the interference from the thermally activated deformation,[38] both nanowires were fully relaxed at 300 K before uniaxial tension straining deformation at an engineering strain rate of $5 \times 10^8\ s^{-1}$.

Local ICO density and its strain evolution

The slabs (20 nm × 40 nm × 6 nm) containing regions of the shear band and necking zone were extracted from the aged and rejuvenated nanowires, respectively, to construct the relationship between structure and deformation mode. To create the density map, we used a 2D Gaussian function to represent each ICO, defined as $\varnothing(x, y, X_i, Y_i, \omega_x, \omega_y) = \frac{1}{2\pi\omega_x\omega_y}\exp\left(-\frac{(x-X_i)^2}{2\omega_x^2} - \frac{(y-Y_i)^2}{2\omega_y^2}\right)$, where (X_i, Y_i) is the i-th ICO atom coordinate, and $\omega_x = \omega_y$ are the Gaussian width in the x- and y-directions, respectively. The distribution of the local ICO density was estimated by $f(x,y) = \sum_{i=1}^{n}\varnothing(x, y, X_i, Y_i, \omega_x, \omega_y)$, where i ranges from 1 to n, and n is the total number of ICOs in the system. Based on the radial distribution functions (Figure S16A), $\omega_x = \omega_y = 2$ was chosen to accurately capture each individual ICO atom and represent the local environment (see Figure S16C). To construct a continuous density map, a mesh-grid with unit size $1 \times 1\ \text{Å}^2$ was established across the sample, with the density value f(x, y) at each unit grid center (x, y) calculated and averaged over the slab thickness (6 nm). An example of the system containing five ICOs is presented in Figures S16D–S16F. To clearly demonstrate the evolution of local ICO density from the initial state in the figure, a fixed color bar range is used for each nanowire at different strain states. The histograms of local ICO density for two nanowires at 0%

strain are shown in Figure S16B, with the complete density evolution with respect to strain shown, for example, in Figure S9.

SUPPLEMENTAL INFORMATION

Supplemental information can be found online at https://doi.org/10.1016/j.matt.2023.01.016.

ACKNOWLEDGMENTS

Y.H., X.L., Z.Z., and J.W. were supported by the National Key R&D Program of China (2021YFA1200201) and the National Natural Science Foundation of China (52071284). H.W., H.C., and P.C. were supported by the US National Science Foundation (CMMI-1935371 and DMR-2105328). R.O.R. was supported by the US Department of Energy, Office of Science, Office of Basic Energy Sciences, Division of Materials Sciences and Engineering (DE-AC02-05CH11231). The authors thank Prof. En Ma and Prof. Jun Ding at Xi'an Jiaotong University for their helpful discussions.

AUTHOR CONTRIBUTIONS

J.W. and P.C. directed the project and designed the experiments. Y.H. and X.L conducted the experiments and analyzed the data. P.C., H.W., and H.C. performed the MD simulations. Y.H., H.W., P.C., and J.W. wrote and revised the paper. R.O.R., L.Z., and Z.Z. contributed to the discussion and paper revision.

DECLARATION OF INTERESTS

The authors declare no competing interests.

Received: September 16, 2022
Revised: November 21, 2022
Accepted: January 20, 2023
Published: February 10, 2023

REFERENCES

1. Hufnagel, T.C., Schuh, C.A., and Falk, M.L. (2016). Deformation of metallic glasses: recent developments in theory, simulations, and experiments. Acta Mater. *109*, 375–393. https://doi.org/10.1016/j.actamat.2016.01.049.

2. Greer, A.L., Cheng, Y.Q., and Ma, E. (2013). Shear bands in metallic glasses. Mater. Sci. Eng. R Rep. *74*, 71–132. https://doi.org/10.1016/j.mser.2013.04.001.

3. Sun, Y., Concustell, A., and Greer, A.L. (2016). Thermomechanical processing of metallic glasses: extending the range of the glassy state. Nat. Rev. Mater. *1*, 16039. https://doi.org/10.1038/natrevmats.2016.39.

4. Jiang, F., Jiang, M.Q., Wang, H.F., Zhao, Y.L., He, L., and Sun, J. (2011). Shear transformation zone volume determining ductile–brittle transition of bulk metallic glasses. Acta Mater. *59*, 2057–2068. https://doi.org/10.1016/j.actamat.2010.12.006.

5. Pan, J., Wang, Y.X., Guo, Q., Zhang, D., Greer, A.L., and Li, Y. (2018). Extreme rejuvenation and softening in a bulk metallic glass. Nat. Commun. *9*, 560. https://doi.org/10.1038/s41467-018-02943-4.

6. Guo, H., Yan, P.F., Wang, Y.B., Tan, J., Zhang, Z.F., Sui, M.L., and Ma, E. (2007). Tensile ductility and necking of metallic glass. Nat. Mater. *6*, 735–739. https://doi.org/10.1038/nmat1984.

7. Jang, D., and Greer, J.R. (2010). Transition from a strong-yet-brittle to a stronger-and-ductile state by size reduction of metallic glasses. Nat. Mater. *9*, 215–219. https://doi.org/10.1038/nmat2622.

8. Yi, J., Wang, W.H., and Lewandowski, J.J. (2015). Sample size and preparation effects on the tensile ductility of Pd-based metallic glass nanowires. Acta Mater. *87*, 1–7. https://doi.org/10.1016/j.actamat.2014.12.039.

9. Magagnosc, D.J., Kumar, G., Schroers, J., Felfer, P., Cairney, J.M., and Gianola, D.S. (2014). Effect of ion irradiation on tensile ductility, strength and fictive temperature in metallic glass nanowires. Acta Mater. *74*, 165–182. https://doi.org/10.1016/j.actamat.2014.04.002.

10. Cockayne, D.J. (2007). The study of nanovolumes of amorphous materials using electron scattering. Annu. Rev. Mater. Res. *37*, 159–187. https://doi.org/10.1146/annurev.matsci.35.082803.103337.

11. Sheng, H.W., Liu, H.Z., Cheng, Y.Q., Wen, J., Lee, P.L., Luo, W.K., Shastri, S.D., and Ma, E. (2007). Polyamorphism in a metallic glass. Nat. Mater. *6*, 192–197. https://doi.org/10.1038/nmat1839.

12. Ma, D., Stoica, A.D., and Wang, X.L. (2009). Power-law scaling and fractal nature of medium-range order in metallic glasses. Nat. Mater. *8*, 30–34. https://doi.org/10.1038/nmat2340.

13. Chen, D.Z., Shi, C.Y., An, Q., Zeng, Q., Mao, W.L., Goddard, W.A., and Greer, J.R. (2015). Fractal atomic-level percolation in metallic glasses. Science *349*, 1306–1310. https://doi.org/10.1126/science.aab1233.

14. Pan, J., Ivanov, Y.P., Zhou, W.H., Li, Y., and Greer, A.L. (2020). Strain-hardening and suppression of shear-banding in rejuvenated bulk metallic glass. Nature *578*, 559–562. https://doi.org/10.1038/s41586-020-2016-3.

15. Sheng, H.W., Luo, W.K., Alamgir, F.M., Bai, J.M., and Ma, E. (2006). Atomic packing and short-to-medium-range order in metallic

glasses. Nature *439*, 419–425. https://doi.org/10.1038/nature04421.

16. Luo, W.K., Sheng, H.W., and Ma, E. (2006). Pair correlation functions and structural building schemes in amorphous alloys. Appl. Phys. Lett. *89*, 131927. https://doi.org/10.1063/1.2356473.

17. Pekin, T.C., Ding, J., Gammer, C., Ozdol, B., Ophus, C., Asta, M., Ritchie, R.O., and Minor, A.M. (2019). Direct measurement of nanostructural change during in situ deformation of a bulk metallic glass. Nat. Commun. *10*, 2445. https://doi.org/10.1038/s41467-019-10416-5.

18. Mu, X., Chellali, M.R., Boltynjuk, E., Gunderov, D., Valiev, R.Z., Hahn, H., Kübel, C., Ivanisenko, Y., and Velasco, L. (2021). Unveiling the local atomic arrangements in the shear band regions of metallic glass. Adv. Mater. *33*, 2007267. https://doi.org/10.1002/adma.202007267.

19. Shao, Y., Yao, K., Li, M., and Liu, X. (2013). Two-zone heterogeneous structure within shear bands of a bulk metallic glass. Appl. Phys. Lett. *103*, 171901. https://doi.org/10.1063/1.4826117.

20. Ding, J., Cheng, Y.Q., and Ma, E. (2014). Full icosahedra dominate local order in Cu64Zr34 metallic glass and supercooled liquid. Acta Mater. *69*, 343–354. https://doi.org/10.1016/j.actamat.2014.02.005.

21. Ma, E. (2015). Tuning order in disorder. Nat. Mater. *14*, 547–552. https://doi.org/10.1038/nmat4300.

22. Nomoto, K., Ceguerra, A.V., Gammer, C., Li, B., Bilal, H., Hohenwarter, A., Gludovatz, B., Eckert, J., Ringer, S.P., and Kruzic, J.J. (2021). Medium-range order dictates local hardness in bulk metallic glasses. Mater. Today *44*, 48–57. https://doi.org/10.1016/j.mattod.2020.10.032.

23. Zhong, L., Wang, J., Sheng, H., Zhang, Z., and Mao, S.X. (2014). Formation of monatomic metallic glasses through ultrafast liquid quenching. Nature *512*, 177–180. https://doi.org/10.1038/nature13617.

24. Liu, S., Wang, L., Ge, J., Wu, Z., Ke, Y., Li, Q., Sun, B., Feng, T., Wu, Y., Wang, J.T., et al. (2020). Deformation-enhanced hierarchical multiscale structure heterogeneity in a Pd-Si bulk metallic glass. Acta Mater. *200*, 42–55. https://doi.org/10.1016/j.actamat.2020.08.077.

25. Sun, J., He, L., Lo, Y.-C., Xu, T., Bi, H., Sun, L., Zhang, Z., Mao, S.X., and Li, J. (2014). Liquid-like pseudoelasticity of sub-10-nm crystalline silver particles. Nat. Mater. *13*, 1007–1012. https://doi.org/10.1038/nmat4105.

26. Hou, Z.Y., Liu, L.X., Liu, R.S., Tian, Z.A., and Wang, J.G. (2010). Short-range and medium-range order in Ca7Mg3 metallic glass. J. Appl. Phys. *107*, 083511. https://doi.org/10.1063/1.3357304.

27. Fan, Y., Iwashita, T., and Egami, T. (2017). Energy landscape-driven non-equilibrium evolution of inherent structure in disordered material. Nat. Commun. *8*, 15417. https://doi.org/10.1038/ncomms15417.

28. Liu, C., Yan, X., Sharma, P., and Fan, Y. (2020). Unraveling the non-monotonic ageing of metallic glasses in the metastability-temperature space. Comput. Mater. Sci. *172*, 109347. https://doi.org/10.1016/j.commatsci.2019.109347.

29. Cheng, Y.Q., and Ma, E. (2011). Atomic-level structure and structure–property relationship in metallic glasses. Prog. Mater. Sci. *56*, 379–473. https://doi.org/10.1016/j.pmatsci.2010.12.002.

30. Spaepen, F. (1977). A microscopic mechanism for steady state inhomogeneous flow in metallic glasses. Acta Metall. *25*, 407–415. https://doi.org/10.1016/0001-6160(77)90232-2.

31. Shi, Y. (2019). Size-dependent mechanical responses of metallic glasses. Int. Mater. Rev. *64*, 163–180. https://doi.org/10.1080/09506608.2018.1476079.

32. Zhao, K., Wang, Y.-J., and Cao, P. (2023). Fracture universality in amorphous nanowires. J. Mech. Phys. Solids, 105210. https://doi.org/10.1016/j.jmps.2023.105210.

33. Wang, C.C., Ding, J., Cheng, Y.Q., Wan, J.C., Tian, L., Sun, J., Shan, Z.W., Li, J., and Ma, E. (2012). Sample size matters for Al88Fe7Gd5 metallic glass: smaller is stronger. Acta Mater. *60*, 5370–5379. https://doi.org/10.1016/j.actamat.2012.06.019.

34. Cao, P., Short, M.P., and Yip, S. (2017). Understanding the mechanisms of amorphous creep through molecular simulation. Proceedings of the National Academy of Sciences *114*, 13631–13636. https://doi.org/10.1073/pnas.1708618114.

35. Cao, P., Short, M.P., and Yip, S. (2019). Potential energy landscape activations governing plastic flows in glass rheology. Proceedings of the National Academy of Sciences *116*, 18790–18797. https://doi.org/10.1073/pnas.190731711.

36. Shanmugam, J., Borisenko, K.B., Chou, Y.-J., and Kirkland, A.I. (2017). eRDF Analyser: an interactive GUI for electron reduced density function analysis. Software *6*, 185–192. https://doi.org/10.1016/j.softx.2017.07.001.

37. Nosé, S. (1984). A molecular dynamics method for simulations in the canonical ensemble. Mol. Phys. *52*, 255–268. https://doi.org/10.1080/00268978400101201.

38. Fan, Y., Iwashita, T., and Egami, T. (2014). How thermally activated deformation starts in metallic glass. Nat. Commun. *5*, 5083. https://doi.org/10.1038/ncomms6083.